

Article

Physics-Based Observers for Measurement-While-Drilling System in Down-the-Hole Drills

Gabriel Bout ¹, Diego Brito ¹ , René Gómez ² , Gonzalo Carvajal ³  and Guillermo Ramírez ^{1,*} 

¹ Departamento de Ingeniería Eléctrica, Universidad Católica de la Santísima Concepción, Concepción 4090541, Chile

² Departamento de Ingeniería Metalúrgica, Universidad de Concepción, Concepción 4070386, Chile

³ Departamento de Electrónica, Universidad Técnica Federico Santa María, Valparaíso 2390123, Chile

* Correspondence: guillermoramirez@ucsc.cl

Abstract: Measurement While Drilling (MWD) is a technology for assessing rock mass conditions by collecting and analyzing data of mechanical drilling variables while the system operates. Nowadays, typical MWD systems rely on physical sensors directly installed on the drill rig. Sensors used in this context must be designed and conditioned for operating in harsh conditions, imposing trade-offs between the complexity, cost, and reliability of the measurement system. This paper presents a methodology for integrating physics-based observers into an MWD system as an alternative to complement or replace traditional physical sensors. The proposed observers leverage mathematical models of the drill's electrical motor and its interaction with dynamic loads to estimate the bit speed and torque in a Down-the-Hole rig using current and voltage measurements taken from the motor power line. Experiments using data collected from four test samples with different rock strengths show a consistent correlation between the rate of penetration and specific energy derived from the observed drilling variables with the ones obtained from standardized tests of uniaxial compressive strength. The simplicity of the setup and results validate the feasibility of the proposed approach to be evaluated as an alternative to reduce the complexity and increase the reliability of MWD systems.



Citation: Bout, G.; Brito, D.; Gómez, R.; Carvajal, G.; Ramírez, G. Physics-Based Observers for Measurement-While-Drilling System in Down-the-Hole Drills. *Mathematics* **2022**, *10*, 4814. <https://doi.org/10.3390/math10244814>

Academic Editor: Mario Versaci

Received: 24 November 2022

Accepted: 15 December 2022

Published: 18 December 2022

Publisher's Note: MDPI stays neutral with regard to jurisdictional claims in published maps and institutional affiliations.



Copyright: © 2022 by the authors. Licensee MDPI, Basel, Switzerland. This article is an open access article distributed under the terms and conditions of the Creative Commons Attribution (CC BY) license (<https://creativecommons.org/licenses/by/4.0/>).

Keywords: measurement while drilling; DTH drilling; physics-based observers; MRAS observer

MSC: 93-05; 93-10; 93B53

1. Introduction

Measurement-while-Drilling (MWD) refers to the process of measuring variables downhole and transmitting them to the surface, typically in near real time, without removing the drill string from down-hole or interrupting the drilling operation [1–4]. Depending on the type of drilling unit and performed task, different types of sensors are incorporated in the bottom-hole assembly (BHA) to measure variables such as thrust, air pressure, feed pressure, percussion pressure, drilling depth, penetration rate, torque, and rotation speed and time, among others [5,6]. These variables provide valuable information for computing different indexes for the rock mass characterization (i.e., variations in rock material, discontinuities, fractures, etc.) [7–9]. The timely collection and processing of these operational variables provide quantitative data for engineering design purposes, facilitate the adequate operation of the drilling equipment to prevent damages from material fatigue and excessive stress, and make the drilling process more efficient [10–12].

Among the measured drilling variables, the rate of penetration (RoP) is one of the metrics that better correlate with the variations of the rock mass. Early works in rock mass characterization while drilling were calculated by measurements of RoP and its relationship with the rock quality index (RQI) [7], rock resistance, and lithology [8]. Later works incorporated other variables such as torque, rotary speed, thrust, flushing medium pressure, and hole length to compute additional indices such as rock fracture index [3], rock

mass P-wave (primary or pressure wave) [10], uniaxial compressive strength (UCS) [11], Brazilian tensile strength, and cohesion and elastic modulus [5].

Another key parameter to determine the properties of the rock mass for optimal design of blast and mine production is the specific energy (SE) [9,13]. The SE is affected by drilling variables (including rotational speed, torque, RoP, and thrust) and rock properties such as rock strength and degree and extension of the fractures [2]. The study detailed in [14] describes the relationship of the SE with the ratio between compressive and shear strength (called K^c factor). The authors in [15] correlated drilling variables and blast performance to the data analysis of different drilling parameters such as hardness coefficient, minimum SE drilling, maximum SE drilling, and specific blasting energy.

Several studies have been carried out for integrating, treating, and interpreting the measurements and indices obtained from MWD systems in different applications. For example, in [16], the authors processed data collected from MWD systems using neural networks and fuzzy logic for rock recognition in blasting applications. The authors in [17] used the collected information from the strata and geological faults to update a 3D geological model. The work in [12] proposed processing MWD readings using machine learning algorithms for the timely detection of operational problems during well-drilling processes, facilitating safe operation and extending the lifetime of drilling equipment. The work reported in [18] described a holistic solution that covers the data acquisition system and data processing algorithms for automatically identifying drilling cycles based on motor current and audio signals.

Typical MWD systems reported in the literature rely on the direct sensing of multiple drilling variables using various sensors located along the drilling rig. To keep the system working correctly, these sensors must be robust to withstand operation in harsh environmental conditions and installed in such a way as to avoid creating additional points of failure for the drilling rig [19]. Moreover, sensors require a transmission medium to send information to the surface, which is particularly challenging for sensors in the BHA [19,20]. Considering the aforementioned challenges, the use of observers, i.e., instances that use mathematical relations to estimate drilling variables using other signals that may be easier to measure, represents a promising alternative for reducing the complexity of the instrumentation required for proper characterization of the rock mass. Observers have been extensively studied and applied in other application domains such as motor control [21–23], motion control [24], electric traction [25,26], and paper making processes [27], among others. However, this approach has yet to be applied to MWD systems.

This paper describes the design and implementation of an MWD system based on robust observers to estimate the rotary speed and torque applied on the drilling surface by a Down-The-Hole (DTH) drilling hammer. The proposed observers estimate the variables of interest using voltage and current measurements taken from the power lines feeding the induction motor that controls the rotational motion in the rotary-percussive DTH drill rig. The observer design considers the physical models that describe the well-known interaction between load torque and induction motor drive, complemented, depending on the case, by state feedback control or adaptive control laws to provide proper stability and command tracking for the estimated variables. According to technical references, DTH hammers operate with impact frequencies ranging from 10 to 28 Hz [28–30], generating high-frequency torsional impacts on the motor shaft, which ultimately generate highly dynamic variations in the magnitude of load torque. Therefore, a relevant objective for this study is to evaluate the ability of the proposed observers to obtain stable estimations of the process variables, considering the highly time-varying loads present during DTH drilling operations. The experimental validation of the proposed observers would enable complementary operation or the removal of physical bit speed and bit torque sensors located in the drilling rig and, by extension, improve the reliability and economic feasibility of MWD systems.

The performance of the proposed observed-based strategy is evaluated by analyzing the data obtained from different rocks and concrete test blocks compared with standardized

UCS tests, which are also correlated with the computed SE. The obtained results show variation ranges from 0.0032 m/s to 0.0103 m/s in RoP, 54.76 Nm to 70.23 Nm in bit torque, and 25.30 MPa to 10.30 MPa in SE when comparing the strongest and the weakest rock grade tested. As expected, the results show that higher values of instantaneous SE match with high-strength rocks represented by higher values of UCS and vice versa.

The reported results provide evidence about the practical utility of observers for lowering the cost and expanding the adoption of MWD technology, which can eventually lead to an increment of the available data to develop and test new techniques for characterizing the rock mass.

2. Materials and Methods

2.1. DTH Drilling System

The DTH drilling system used for this study consists of an induction motor as a primary rotary actuator that drives the rotary bit through a gearbox (rotary head). A pneumatic control console distributes high-pressure air from the rotary screw compressor to the feed mechanism and DTH hammer for percussion and hole cleaning. Table 1 summarizes the main technical specifications of the experimental drill rig implemented for this study, and Figure 1 shows the main components and their interconnections. In the figure, the yellow arrows indicate the air pressure lines interconnections, the green arrows indicate the location of a pressure sensor and a depth sensor for direct measurement of operational variables, and the light blue arrows indicate the location of the power line terminals at the drill motor end. The voltage and current of the motor are three-phase signals measured at the output of the power converter that supplies power to the motor (not shown in the figure) and are used to estimate the torque and compute the SE. All readings from the sensors are collected and processed in a dedicated data acquisition (DAQ) system with advanced processing capabilities that enable the implementation of different observer algorithms.

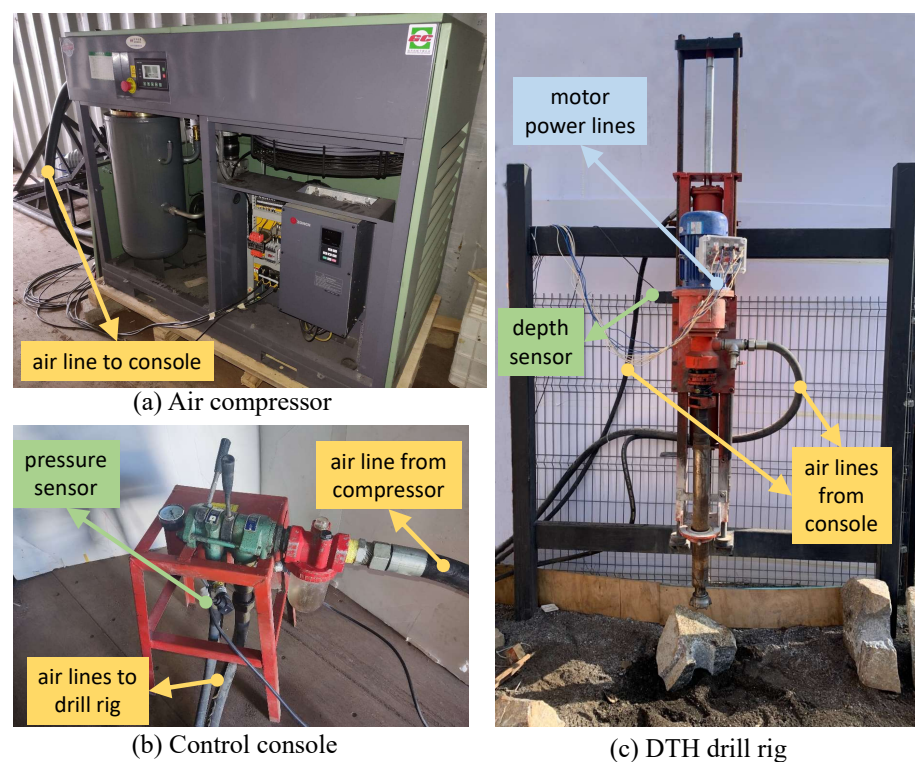


Figure 1. DTH drilling setup including main components and their interconnections.

Table 1. DTH Drilling system specifications.

Item	Value
Hole diameter	90–130 mm
Working pressure	0.5–1.0 Mpa
Air consumption	6 m ³ /min
Motor power	4 kW
Motor speed	1440 rpm
Motor voltage	380 V
Compressor power	37 kW
Compressor pressure	0.8 Mpa
Gearbox reduction ratio	11
Bit speed	90 rpm

2.2. Observer-Based MWD System

The MWD system proposed for this study combines physical sensors and observers to simplify the instrumentation required for rock mass characterization. Figure 2 shows a general interconnection diagram for the designed solution, using different color lines and boxes to illustrate the signal flow for the different sensors, including the hammer pressure sensor (P_h), drilling depth sensor (D), motor voltage sensor (V), and motor current sensor (I). In the figure and the rest of the document, the symbol $\hat{}$ above a variable indicates an estimated variable.

Table 2 summarizes the technical specifications for the sensors used in this study. Voltage and current sensors are installed in the power lines from the power converter to the motor, while the depth sensor is installed in the drill rig. The P_h sensor is installed in the pneumatic console, and, in this case, it is monitored to ensure that the pneumatic system is operating within safe ranges. All sensor readings are filtered and conditioned in the DAQ and signal processing unit (MicroLabBox processor [31]) and then used to estimate drilling variables.

The V and I signals measured at the power converter are used to estimate the bit speed ($\hat{\omega}_b$) and bit torque (\hat{T}_b) using a chain of observers. In Figure 2, the data flow for the observers is marked with red arrows and boxes. Voltage and current are three-phase signals that are converted to qd components through Clark's transformation (stationary reference frame) before entering the observers. For simplicity, this step is omitted in the diagram. First, the rotor speed model reference adaptive system (MRAS) observer uses the V and I readings to estimate the rotor speed ($\hat{\omega}_r$). Using $\hat{\omega}_r$ and the measured values of V and I , another observer estimates the rotor flux linkages ($\hat{\lambda}_r$). Finally, the last observer in the chain uses $\hat{\omega}_r$ and $\hat{\lambda}_r$ together with the measured I to estimate both $\hat{\omega}_b$ and \hat{T}_b . The design of these observers is described in detail in Section 2.3.

The green path represents the computation of the RoP obtained as the derivative of the D sensor in time. The RoP is later used to compute the SE (in J/m³), which represents the ratio between the energy involved during the drilling process and the volume of material drilled, being defined as:

$$SE = \frac{F_b}{A} + \frac{\hat{\omega}_b \times \hat{T}_b}{A \times \text{RoP}} \quad (1)$$

where F_b is the bit thrust force measured in N, A is the drilled area or bit surface measured in m², $\hat{\omega}_b$ is in rad/s, \hat{T}_b is in Nm, and the RoP is measured in m/s. For this study, F_b is kept constant at 1623.86 N (given by the mass of the mobile drilling structure itself).

The observed-based MWD system is completed with a graphic display implemented on a computer equipped with the ControlDesk software used to configure the signal data acquisition and for real-time display.

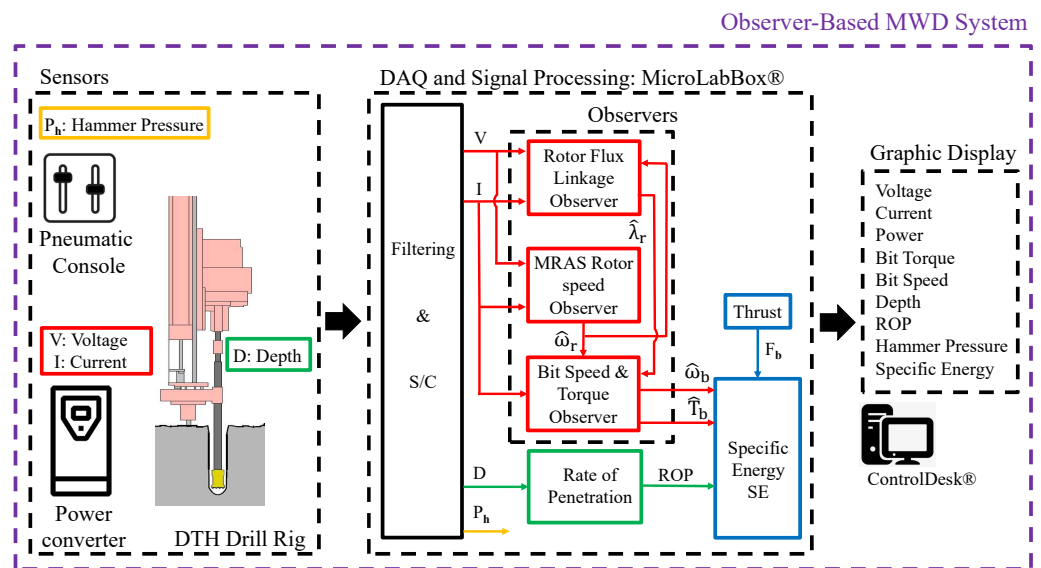


Figure 2. Schematic diagram of the proposed observer-based MWD system.

Table 2. MWD sensor specifications.

Sensor type	Quantity	Range	Output
Voltage diff. probe	3	DC + AC peak: 1000 V	+/-5.0 V
Current clamp	3	DC + AC peak: 30 A	+/-100 mV/A
Depth (TOF laser)	1	0.25–2.5 m	0–10 V
Hammer pressure	1	0–10 bar	0–10V

2.3. Observers Design

The design of the different observers in this application is based on the physical models that govern the behavior of induction motors interacting with dynamic loads. Implementing these models requires identifying the resistances and inductances of the motor stator, magnetizing branch, and rotor.

For this study, these parameters were obtained from the motor identification routine performed via software available for motor converters [32]. The obtained parameters and motor specifications are summarized in Table 3.

Table 3. Induction motor parameters.

Parameter	Value
Rated power	4 kW
Rated speed	1440 rpm
Rated voltage	380 V
Rated frequency	50 Hz
Stator resistance (R_s)	1.3809 Ω
Rotor resistance (R_r)	0.6843 Ω
Stator leakage inductance (L_{ls})	0.1670 H
Rotor leakage inductance (L_{lr})	0.1675 H
Magnetizing inductance (L_m)	158.37 mH

2.3.1. MRAS Back-EMF Rotor Speed Observer

The first observer in the proposed MWD system is the MRAS Back ElectroMotive Force (BEMF) speed observer used to obtain $\hat{\omega}_r$. In this study, the MRAS-BEMF observer is chosen to avoid problems with pure integration associated with the more commonly used MRAS estimator based on rotor flux models [33,34]. Figure 3 shows the block diagram of the implemented MRAS-BEMF rotor speed observer, derived from equations of the three-phase induction motor dynamic model after applying Clarke’s transformation resulting in a two-phase model ($d - q$ coordinates) in a stationary reference frame. To estimate the rotor

speed, the observer uses a reference model (known as the voltage model) that does not include the speed estimate. In contrast, the adjustable model (known as the current model) includes speed estimates. For this and the following observers, the parameters denoted by R represent resistances, and parameters denoted by L represent inductances, while the subscripts $s, m,$ and r denote stator, magnetizing branch, and rotor parameters, respectively. Moreover, combinations of resistances and inductances generate time constants represented by T , while σ denotes the leakage coefficient. Some of these parameters can be directly obtained from Table 3. Detailed specifications for each parameter can be found in [33].

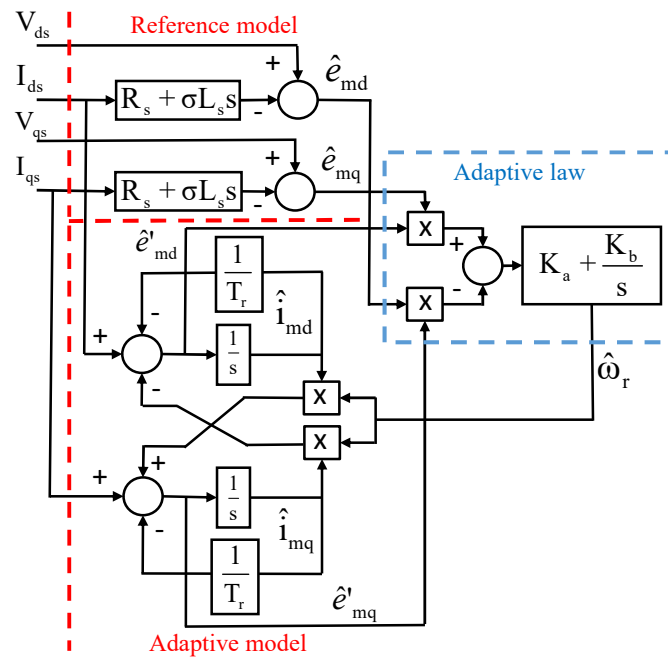


Figure 3. Block diagram of the MRAS Back-EMF rotor speed observer (from [34]).

2.3.2. Rotor Flux Linkage Observer

A flux linkage is defined as the product of the number of turns in a coil and the magnetic flux passing through the coil. For induction motors, this variable is required to estimate the instantaneous electromagnetic torque developed by the machine. There are several methods to estimate rotor flux linkage space vector ($\hat{\lambda}_r$). The model chosen for this study is the rotor flux model described in [35], considering its insensibility to changes in motor parameters influenced by temperature. Figure 4 shows the block diagram of the RFLO. Again, this model is derived from the induction motor dynamic two-phase model ($d - q$ coordinates) in a stationary reference frame. It should be noted that this observer requires the rotor speed signal, which is estimated by the MRAS-BEMF rotor speed observer previously described using the same nomenclature.

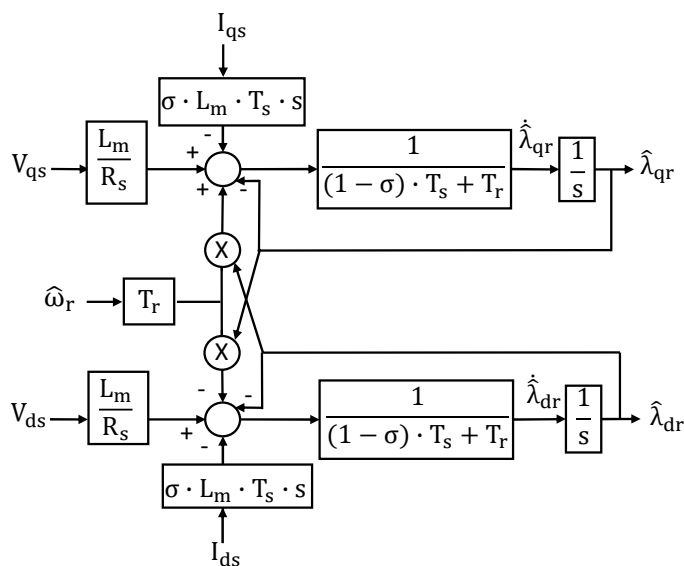


Figure 4. Block diagram of the rotor flux linkage observer (build from [35]).

2.3.3. Bit Speed and Torque Observer

The last observer required for the proposed MWD system is the Bit Speed and Torque Observer (BSTO). The block diagram of this observer is shown in Figure 5 and is based on the velocity observer described in [27], designed for papermaking applications. This BSTO estimates the bit torque within the observer bandwidth and can be seen as a (disturbance) state filter where lagging can be significantly near or above the observer bandwidth. The BSTO uses the estimated rotor speed scaled from the MRAS BEMF observer to obtain the estimated motor speed ($\hat{\omega}_m = \hat{\omega}_r / \text{number of pole pairs}$), which is then converted to estimated bit speed ($\hat{\omega}_b$) through the gearbox reduction ratio GR (see Table 1) as shown in the following equation:

$$\hat{\omega}_b = \hat{\omega}_r \times \frac{2}{P \times GR} \tag{2}$$

where P is the number of poles of the motor.

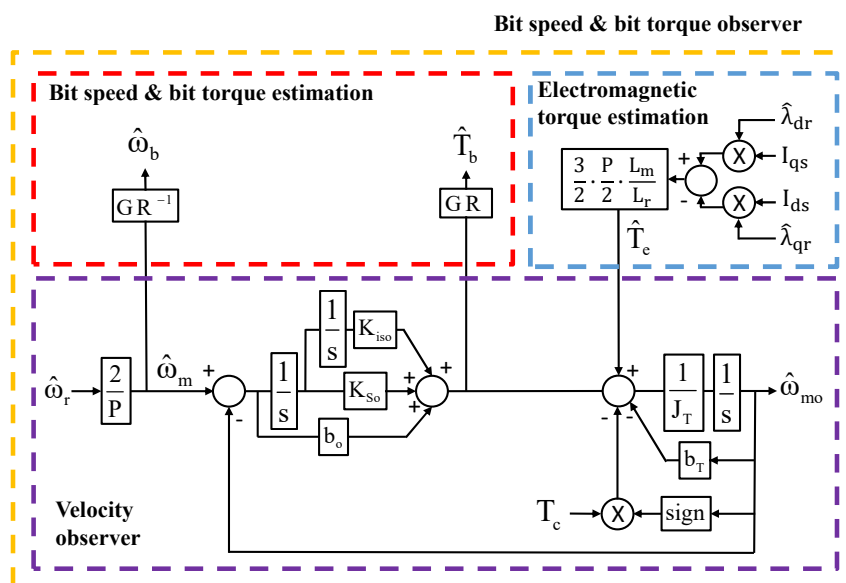


Figure 5. Block diagram of the bit speed and bit torque observer.

This observer also requires the estimation of electromagnetic torque (\hat{T}_e) acting as a feed-forward signal. In this case, the \hat{T}_e can be calculated as:

$$\hat{T}_e = \frac{3}{2} \frac{P}{2} \frac{L_m}{L_r} \times (\hat{\lambda}_{dr} I_{qs} - \hat{\lambda}_{qr} I_{ds}) \tag{3}$$

According to Figure 5, the resulting bit torque (\hat{T}_b) has a negative sign and, therefore, should be multiplied by -1 to obtain a positive value.

The mechanical parameters of the BSTO J_T , b_T , and T_c represent the total inertia, total viscous drag, and the Coulomb friction, respectively. The J_T is the sum of all components individual inertia (motor, gear reducer, and hammer inertia), while b_T is the sum of the motor and gear reducer viscous drag. The Coulomb friction is an approximate model used to calculate the force of dry friction, and in this case, its constant value reached 1.7 Nm. All these parameters can be calculated from the T_e vs. ω_m curve obtained from acceleration ramps and steady operation under no load conditions [36]. Table 4 summarizes the mechanical parameters of the drill rig obtained from experimental tests.

Table 4. Mechanical parameters of drill rig.

Parameter	Value
Total inertia	0.0244 Kg m ²
Total viscous drag coefficient	0.0100 Nms/rad
Static friction	1.7 Nm

3. Results

In this section, the proposed observer-based MWD system is experimentally evaluated considering four different drilling testing specimens with different compositions that cover a wide range of compressive strengths. The objective of the experiments is to assess the correlation of the estimated drilling variables $\hat{\omega}_b$, \hat{T}_b , and SE with the properties of the specimens.

3.1. Drilling Testing Specimens

Figure 6 shows referential pictures of the four types of specimens evaluated in the experiments, including rocks collected from local quarries and concrete blocks with different compositions. The characteristics of the specimens used in the experiments are summarized below:

- Specimen of type (a) is a high hardness tonalite (granite) phaneritic crystalline formed by plagioclase (large crystals), quartz, biotite, and hornblende. The approximate dimensions of the testing samples are 300 mm × 700 mm × 400 mm (height × width × depth).
- Specimen of type (b) is a metamorphic rock from a pelitic protolith presenting foliation between slate and schistoseis. The approximate dimensions of the testing samples are 200 mm × 500 mm × 300 mm (height × width × depth)
- Specimen of type (c) is a concrete block composed of 55% of concrete type H-25 (compressive strength ≥ 25 MPa) and 45% of gravel of one inch or smaller size. The approximate dimensions of the testing samples are 300 mm × 300 mm × 300 mm (height × width × depth)
- Specimen (d) is concrete H-10 (compressive strength ≥ 10 MPa). Sample dimensions are similar to specimen c.

For purposes of laboratory characterization, the four specimens were subjected to the standard test method of uniaxial compressive strength (UCS) [37] using a hydraulic press machine (Matest C089). The rock and concrete cores tested were obtained directly from the rock and concrete samples. The cores were prepared based on the ASTM D4543 standard, applying a vertical load and registering the measured load and vertical displacement until core breakage. Table 5 shows the UCS results for the specimens, including the rock grade

and classification reported in [38]. It can be seen that the testing specimens cover a wide range of rock strengths, from very strong to (equivalent) weak rocks for concrete blocks. The table also includes an identifier for each specimen based on the particular properties, which will be used in the rest of the document to refer to each sample.

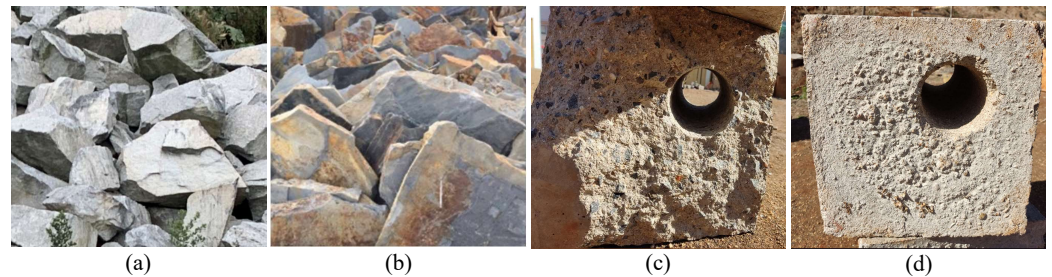


Figure 6. Rock and concrete specimens for evaluation of observer-based MWD system: (a) quarry rock 1; (b) quarry rock 2; (c) concrete/gravel block 1; (d) concrete block 2.

Table 5. Laboratory results of UCS for testing specimens.

Specimen	UCS (MPa)	Classification (Grade)	Identifier
Quarry rock (a)	161.51 ± 11.54	Very strong (R5)	QR-R5
Quarry rock (b)	92.64 ± 42.89	Strong (R4)	QR-R4
Concrete block with gravel (c)	25.42 ± 1.43	Medium strong (R3)	CB-R3
Pure concrete block (d)	14.54 ± 3.65	Weak (R2)	CB-R2

3.2. Estimation of Rotor Flux

Figure 7 shows the qd components of the stator current (a) and voltage (b) input signal in a rotating reference frame along with the estimated output rotor flux linkages qd components generated by the RFLO (c). The measured V and I correspond to no-load operation at a speed of 1440 rpm on the motor side. Voltage components are not pure sinusoidal since they are obtained from a pulse width modulated (PWM) converter after a low pass filter stage set at 500 Hz. Current components are filtered similarly, reaching a peak close to 3.2 A for both qd components. Finally, based on measured voltages and currents combined with the motor equivalent circuit parameters, the resulting flux linkage output signals are estimated, reaching an amplitude around 2 Wb-t and showing an expected 90° phase offset between qd components, in the same way as voltage and current signals. It should be noted that $\hat{\omega}_r$ is a required input signal for the RFLO that comes from the MRAS-BEMF rotor speed observer. The tuning of the adaptive mechanism (K_a and K_b gains) for the MRAS-BEMF observer imposes a trade-off between fast response and high noise and disturbances rejection. Detailed descriptions of features, including dynamic tracking performance and stability analysis, can be found in [33,34]. The evaluation of the MRAS-BEMF observer is described by integrating $\hat{\omega}_r$ as the input signal (speed reference) for the BSTO. In the same way, the flux linkage signals estimated for the RFLO are subsequently incorporated as input signals for the electromagnetic torque estimation T_e required for the proper operation of BSTO as shown in Section 2.3.3.

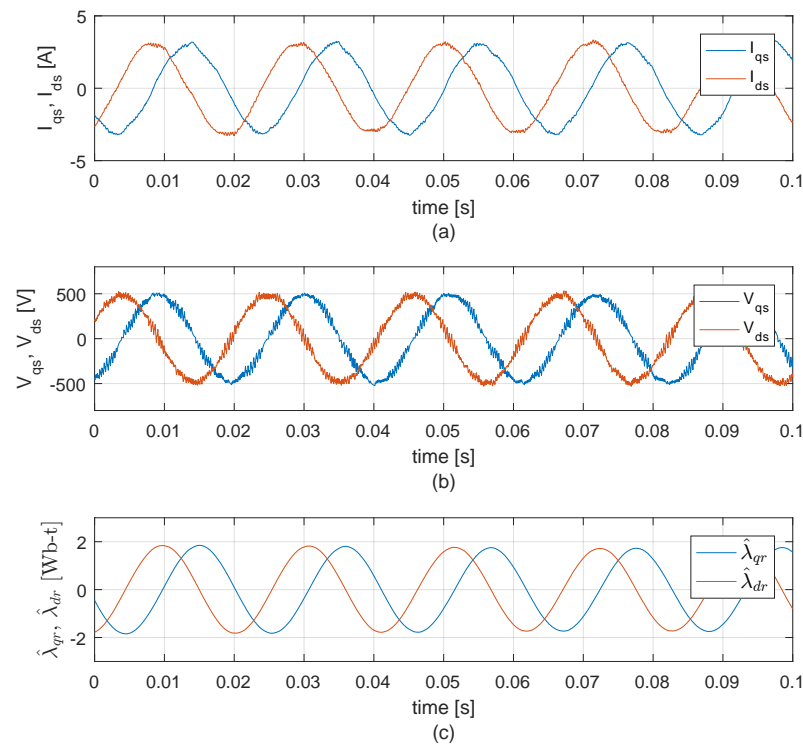


Figure 7. Evaluation of RFLO under no load conditionL (a) *qd* current components; (b) *qd* voltage components; (c) *qd* estimated rotor flux linkage components.

3.3. Bit Speed and Torque Estimation

To assess the operation of the BSTO, the experimental evaluation considers a typical motor starting cycle beginning at time 10 s with a speed ramp that reaches the rated speed (load side) of 90 rpm at 15 s and then continues operating at a constant speed. Then, around $t = 35$ s, the drilling operation of a QR-R5 (see Table 5) starts, stopping later at time $t = 97$ s when the testing specimen is completely traversed. To facilitate the analysis, in the following figures, the inputs variables ($\hat{\omega}_m$ and \hat{T}_e) of the BSTO are shown referred to the bit side. According to Figure 5, it should be noted that the referred input speed signal $\hat{\omega}_m$ is equivalent to $\hat{\omega}_b (= \hat{\omega}_m / GR)$. To evaluate the effect of bandwidth tuning of the BSTO (in practice, this selection is user defined), two different values are considered: (i) $b_o = 0.3$ Hz, $k_{s_o} = 0.048$ Hz, and $k_{i_{s_o}} = 0.006$ Hz; and (ii) $b_o = 25$ Hz, $k_{s_o} = 4$ Hz, and $k_{i_{s_o}} = 0.5$ Hz.

Figure 8 shows the observer performance considering a bandwidth of case (i). This figure shows that the observer speed tracking is poor, especially when drilling starts and stops ($t = 35$ s and $t = 97$ s, respectively). However, the bit torque component (\hat{T}_b) of the electromagnetic torque is adequately isolated from friction and inertial components. This relatively low bandwidth produces a significant filtering effect showing negligible magnitude oscillations for \hat{T}_b but with a significant lagging impact. Thus, if better speed tracking is desirable, the observer bandwidth should be incremented.

Figure 9 shows observer performance when case (ii) is selected. In this case, both observer speed output $\hat{\omega}_{m_o}$ and bit torque have proper tracking properties; however, \hat{T}_b has a higher oscillatory component but lower lagging when compared with the previous lower observer bandwidth case. Regarding the \hat{T}_b profile, Figures 8 and 9 show that during the drilling operation, two stages can be distinguished. First, from $t = 35$ s, the drill bit penetrates the testing specimen, and the bit torque increases linearly until $t = 45$ s. Then, the bit torque is kept practically constant, developing almost 55 Nm, until the rock specimen is completely traversed around $t = 97$ s when the bit torque falls to zero.

Figures 8 and 9 demonstrate that the proposed BSTO can isolate the drilling torque component from frictional and inertial components present in the mechanical system, even

when low bandwidth is set. Therefore, the bandwidth choice is a user option that sets a trade-off between filtering and lagging properties when \hat{T}_b is the target signal.

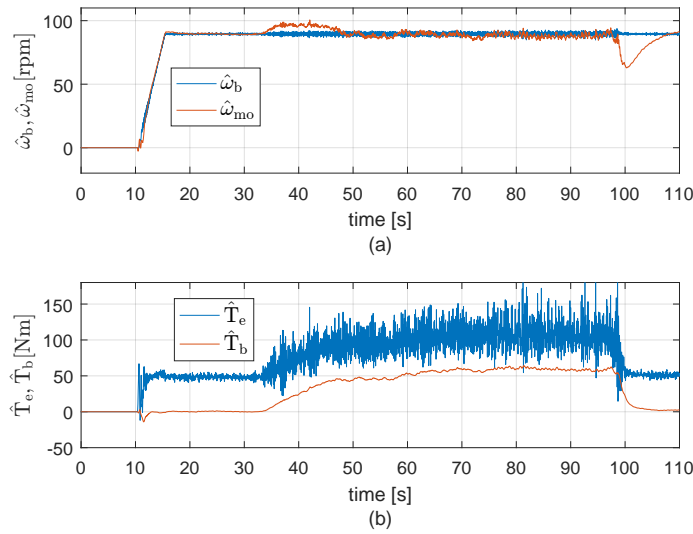


Figure 8. Evaluation of BSTO under drilling condition, considering low bandwidth observer tuning: (a) $\hat{\omega}_{mo}$ referred to bit side; (b) \hat{T}_e referred to bit side.

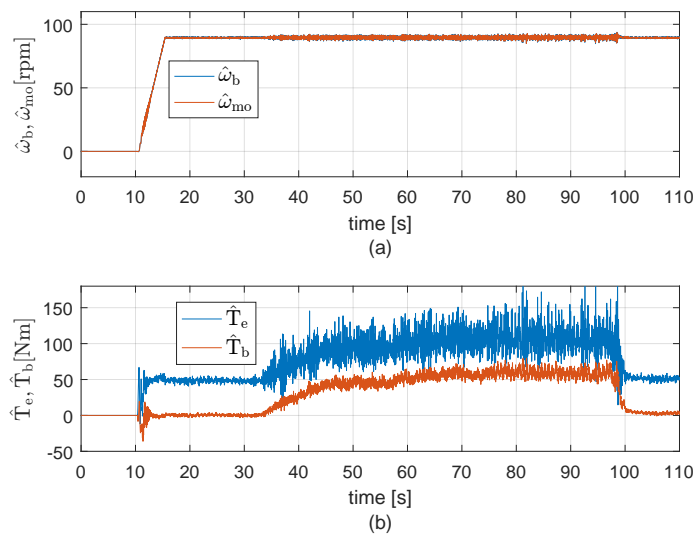


Figure 9. Evaluation of BSTO under drilling condition, considering proper bandwidth observer tuning: (a) $\hat{\omega}_{mo}$ referred to bit side; (b) \hat{T}_e referred to bit side.

3.4. Evaluation of the Observer-based MWD System

Considering the four testing specimens previously described, the next step in this study is the experimental evaluation of the overall performance of the observer-based MWD system, including measured and estimated variables. To evaluate the performance under significantly different drilling materials, the cases of QR-R4 and CB-R2 are selected for detailed analysis, including the collected signals coming from both sensors and observers. Figure 10 shows the signals obtained from physical sensors that include depth, RoP, and hammer pressure. Figure 11 shows the observer-based signals of bit speed, bit torque, and the specific energy considering the drilling operation of QR-R4.

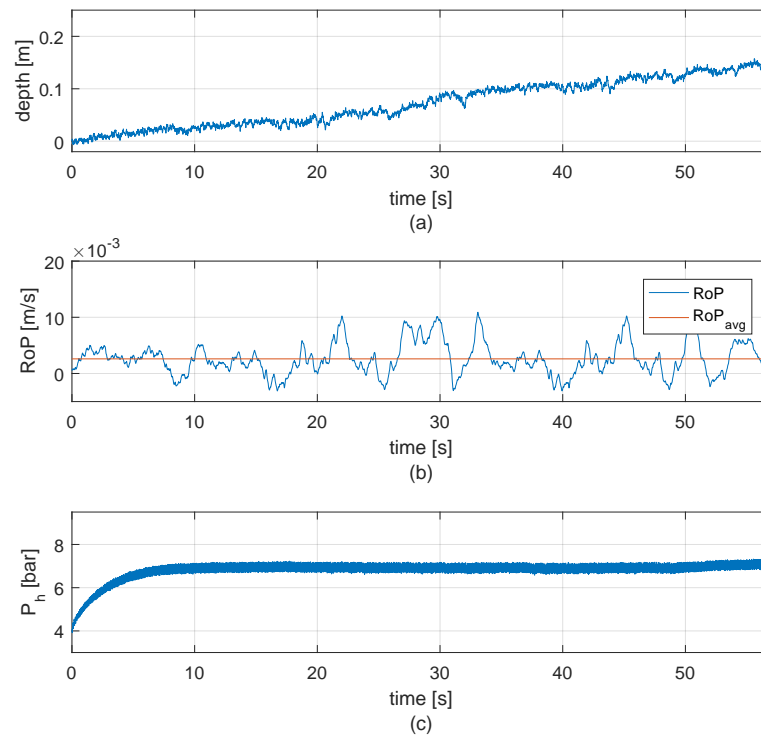


Figure 10. Evaluation of observer-based MWD system during drilling condition of QR-R4, measured variables: (a) depth; (b) RoP and average RoP; (c) P_h .

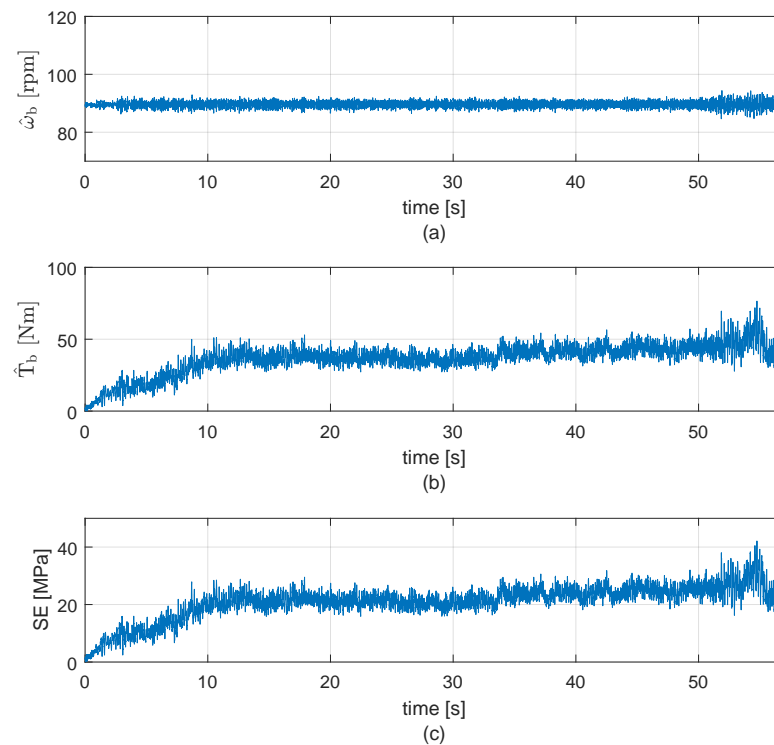


Figure 11. Evaluation of observer-based MWD system during drilling condition of QR-R4, estimated variables: (a) $\hat{\omega}_b$; (b) \hat{T}_b ; (c) SE .

Figure 10a shows that the total depth for the sample test QR-R4 reached 15.6 cm in a period of 56.9 s, giving an average RoP of 0.0026 m/s (see Figure 10b). In Figure 10c, the hammer pressure is stabilized at $t = 10$ s, approximately after the bit is entirely in the rock sample. Recall that the P_h signal is monitored for the safe operation of the pneumatic system but also allows us to observe the start and end time of the drilling operation along with the

magnitude evolution required for comparative analysis of different specimens. Figure 11a, shows that the estimated bit speed is nearly constant at 90 rpm during the drilling period; however, the estimated bit torque component increased from 0 to 40.6 Nm at $t = 11.84$ s to then stay nearly constant until the end of the evaluation (see Figure 11b). Figure 11c shows the specific energy calculated from Equation (1), considering the average RoP to avoid an excessively noisy signal. The SE, in this case, reached an average of 23.2 MPa during steady drilling operation (after $t = 10$ s). These results show that when the drilling specimen is uniformly composed, the \hat{T}_b develops a nearly constant shape after the bit is completely inserted in the drilled material, and therefore the resulting SE follows the same behavior when a steady RoP is assumed. Thus, it would be possible to establish ranges of operation for both \hat{T}_b and SE for different rock mass being drilled when the same drill rig machine and bit are used.

Figure 12 shows the signals obtained from physical sensors of depth, RoP, and hammer pressure, while Figure 13 shows the observer-based signals of bit speed, bit torque, and the specific energy considering drilling operation of CB-R2. Compared with the previous case (Figure 10a), the total depth is almost double, reaching 32.4 cm but with a shorter drilling period of 29.6 s. As a result, the average RoP is 0.0103 m/s, representing about four times the RoP obtained for the previous case. Figure 12c shows that this test was performed with a similar hammer pressure (around 6.8 bar in steady state) than the previous case. Looking at Figure 13b, the bit torque reached 70.23 Nm during steady operation (after $t = 10$ s), representing an increment of 72% when compared with Figure 11b. Considering that this case represents the drilling of the weakest test sample, the resulting specific energy was 10.3 MPa, representing 44% of the SE obtained for the stronger QR-R4.

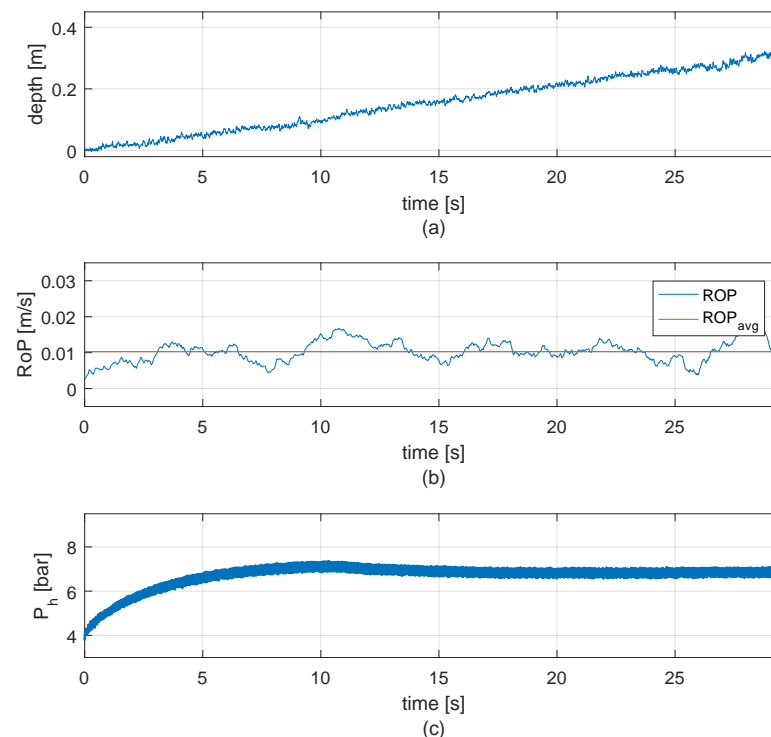


Figure 12. Evaluation of observer-based MWD system during drilling condition of block 2, measured variables: (a) depth; (b) RoP and average RoP; (c) P_h .

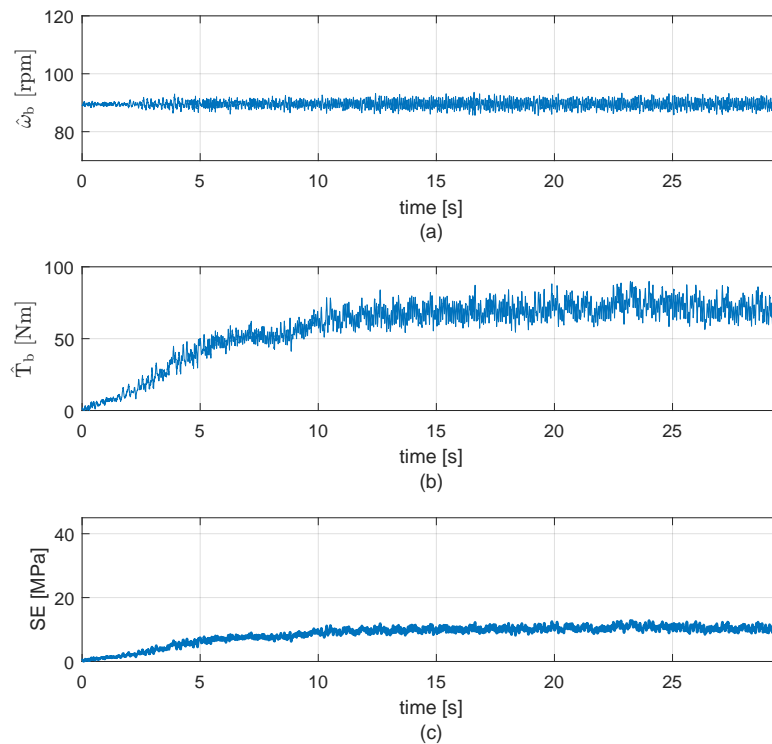


Figure 13. Evaluation of observer-based MWD system during drilling condition of block 2, estimated variables: (a) $\hat{\omega}_b$; (b) \hat{T}_b ; (c) SE .

Following the same evaluation procedure described in Figures 10–13, Table 6 summarizes the results of RoP, \hat{T}_b , and SE for the four testing specimens. The results of UCS (shown in Table 5) are also included to facilitate the analysis. The results summarized in Table 6 show a correlation between the average SE and the UCS. Although this correlation is not proportional, it is clear that SE computed by the observer-based MWD system increases when the UCS of the testing sample increases. Regarding the average RoP, CB-R2 has the highest value since this concrete block has the weakest sample classification according to its UCS value. Consequently, although the CB-R2 specimen has the highest bit torque with the highest RoP, the SE reaches the lowest values among the four samples. Both QR-R5 and QR-R4 specimens represent particular cases. In the case of QR-R5, the combination of a high bit torque and relatively low RoP results in the highest specific energy. On the other hand, QR-R4 has the lowest RoP but, combined with lower bit torque compared to QR-R5, results in the second highest SE value.

Table 6. Experimental results of average RoP , average steady \hat{T}_b , average steady SE and UCS for 4 testing specimens.

Specimen	RoP_{avg} [m/s]	$\hat{T}_{b,avg}$ [Nm]	SE_{avg} [MPa]	UCS [MPa]
QR-R5	0.0032	54.76	25.30	161.51
QR-R4	0.0026	40.57	23.24	92.64
CB-R3	0.0054	60.39	16.85	25.42
CB-R2	0.0103	70.23	10.30	14.54

4. Discussion

The proposed observer for the bit speed and bit torque observer incorporates the estimations of the rotor speed from the MRAS-BEMF observer and the electromagnetic torque that uses rotor flux linkage estimates coming from RFLO. Therefore, considering an application perspective, we can focus on the outputs of the BSTO to evaluate the interactions between different estimated variables and their stable tracking under no-load conditions and dynamic load torque. The highly time-varying load condition typical in the

target operational scenarios is evidenced in Figure 8b, where the estimated electromagnetic torque presents high oscillations during the drilling operation, reaching variations in its magnitude of up to 120 Nm (from 50 to 170 Nm around $t = 82$ s). The results show that, despite these dynamic oscillations, all variables interacting in the BSTO converge to a stable behavior and generate stable estimations for bit speed and bit torque, demonstrating that a proper use of MRAS and feedback control engineering tools allow stable observer tracking of drilling variables under different operational scenarios.

As mentioned in Section 2.3.3, the bandwidth of the BSTO is a user-specified parameter that represents a trade-off between the tracking error in the estimated bit speed $\hat{\omega}_{mo}$ and the noise and delay on the estimated bit torque. In general, a high-bandwidth configuration for the BSTO will provide low tracking error in the $\hat{\omega}_{mo}$ signal of the velocity observer (framed by the purple dashed line in Figure 5) but a noisy torque estimation. On the other hand, a low-bandwidth configuration will degrade the tracking error in the $\hat{\omega}_{mo}$ signal but produce a smooth torque estimation with an additional delay compared to the estimation with low bandwidth configuration. At this point, it is important to note that the $\hat{\omega}_{mo}$ is an internal signal that is only used for estimating the bit torque, while the actual bit speed output $\hat{\omega}_b$ of the BSTO is obtained from the MRAS-BEMF observer. Therefore, from an application perspective, a low bandwidth tuning can be perfectly acceptable for practitioners focused on the estimation of a smooth bit torque component with a tolerable lag, despite the expected degradation in the speed tracking.

The results obtained from the experiments on the testing specimens show that, as expected, the drilling of stronger rocks produces lower RoP compared to weaker blocks; however, the bit torque has an opposite behavior, increasing its magnitude when drilling weaker rocks. The SE index incorporates these variables and shows a clear correlation with the UCS index for all tested samples, consistent with the specialized literature. The experiments show that the observer-based system can track variations in the bit torque and specific energy at different stages of drilling a single specimen. Moreover, the average magnitude of the monitored variables shows significant relative variations among the different testing specimens. Therefore, it is reasonable to expect that the proposed system can identify changes in the lithology along the borehole in deep drilling operations.

In this study, the RoP signal is computed as the simple derivative of the depth sensor readings with respect to time, considering fixed sampling intervals. In practice, the depth readings are expected to be noisy due to the intrinsic vibration in the system components during the drilling operations. Using a simple derivative algorithm, the variations in the depth readings produce an oscillating instantaneous RoP, even generating non-physical negative values when drilling high-strength rock due to higher vibrations (see Figure 10). Although we circumvent this problem by using the average RoP over a time window, it would be interesting to test improved algorithms that take into consideration the effect of rock strength (rocks with higher strength generate more vibration than weaker rocks) in the RoP estimation, avoiding non-physical estimations without adding excessive delay.

The overall results show that the proposed observer-based measurement system can effectively estimate the bit rotational speed and bit torque of a DTH drilling rig using measurements of current and voltages taken from the motor power lines, which are normally located in safe cabinets that are easy to access and do not require specialized telemetry. The observers can either operate in redundancy with physical bit torque and bit speed sensors located in the drilling rig to increase the reliability of the MWD system or replace physical sensors to simplify the required instrumentation and reduce deployment and operational costs. To the best of our knowledge, this is the first study reporting evidence about the effectiveness of observers in MWD systems for estimating indexes for rock mass characterization. Although the proposed topology is implemented and tested in a laboratory setup, the presented methodology for the design, tuning, and implementation of the observers follows logical steps that can be directly adapted for industrial settings.

5. Conclusions

This study presents the design and evaluation of an observed-based MWD system. The proposed system comprises three observers that used physics-based models of motor dynamics to estimate the bit rotational speed and bit torque in a down-the-hole drilling rig using measurements of current and voltage taken at the motor power line, away from the harsh drilling operational environment. The estimated variables are then combined with the rate of penetration derived from a physical depth sensor to obtain the specific energy associated with the drilling process.

The performance of the proposed observer-based MWD system is evaluated by analyzing the variables estimated during the drilling of different testing specimens with different rock strengths, covering from very strong to weak rocks according to the UCS index. Experimental results showed that the observers reached stable responses under both no-load conditions and rapid variations in the load torque derived from high-frequency torsional impacts in the motor shaft that typically occur during DTH drilling. Moreover, the on-field computed value of specific energy obtained using the observed variables showed a consistent correlation with the off-line laboratory results for the UCS, which is one of the most representative parameters for rock mechanic characterization.

By providing evidence about the utility of observers for complementing or replacing traditional physical sensors located on a drilling rig, we expect the results will provide a baseline for further studies oriented to increase the reliability and economic feasibility of MWD systems. Advances in this area can also increase the quantity and quality of data available for performing exhaustive data-driven analysis in rock mass characterization and intelligent process monitoring, which would lead to improvements in engineering calculations and timely decision making during rock excavation procedures in mining, construction, and oil, among other industries.

Author Contributions: Conceptualization, G.R. and R.G.; methodology, G.R. and R.G.; software, G.B. and D.B.; validation, G.B., D.B., R.G. and G.R.; formal analysis, G.R., R.G. and G.C.; investigation, G.R., G.B., D.B. and G.C.; writing—original draft preparation, G.R., G.C. and R.G.; writing—review and editing, G.R. and G.C.; visualization, G.R., G.C. and R.G.; supervision, G.R.; project administration, G.R.; funding acquisition, G.R. All authors have read and agreed to the published version of the manuscript.

Funding: This work was funded by the National Agency for Research and Development (Agencia Nacional de Investigación y Desarrollo ANID) through project FONDECYT 11180768.

Institutional Review Board Statement: Not applicable.

Informed Consent Statement: Not applicable.

Acknowledgments: Not applicable.

Conflicts of Interest: The authors declare no conflict of interest.

References

1. Gooneratne, C.P.; Li, B.; Deffenbaugh, M.; Moellendick, T. *Instruments Measurement Principles and Communication Technologies for Downhole Drilling Environments*, 1st ed.; Springer: Cham, Switzerland, 2019.
2. Khorzoughi, M.B.; Hall, R. Processing of measurement while drilling data for rock mass characterization. *Int. J. Min. Sci. Technol.* **2016**, *26*, 989–994. [[CrossRef](#)]
3. Navarro, J.; Segarra, P.; Sanchidrián, J.; Castedo, R.; Pérez Fortes, A.; Natale, M.; Lopez, L. Application of an in-house MWD system for quarry blasting. In Proceedings of the 12th International Symposium on Rock Fragmentation by Blasting, Luleå, Sweden, 11–13 June 2018.
4. Isheyskiy, V.; Sanchidrián, J.A. Prospects of Applying MWD Technology for Quality Management of Drilling and Blasting Operations at Mining Enterprises. *Minerals* **2020**, *10*, 925. [[CrossRef](#)]
5. Liu, C.; Zheng, X.; Shahani, N.M.; Li, P.; Wang, C.; Guo, X. An Experimental Investigation into the Borehole Drilling and Strata Characteristics. *PLoS ONE* **2021**, *16*, e0253663. [[CrossRef](#)] [[PubMed](#)]
6. Gooneratne, C.P.; Li, B.; Moellendick, T.E. Downhole Applications of Magnetic Sensors. *Sensors* **2017**, *17*, 2384. [[CrossRef](#)]
7. Leighton, J.C. Development of a Correlation between Rotary Drill Performance and Controlled Blasting Powder Factors. Master's Thesis, University of British Columbia, Vancouver, Canada, 1982.

8. Scoble, M.J.; Peck, J. A technique for ground characterization using automated production drill monitoring. *Int. J. Surf. Min. Reclam. Environ.* **1987**, *1*, 41–54. [[CrossRef](#)]
9. Khorzoughi, M.B.; Hall, R. Rock fracture density characterization using measurement while drilling (MWD) techniques. *Int. J. Min. Sci. Technol.* **2018**, *28*, 859–864. [[CrossRef](#)]
10. Basarir, H. Prediction of rock mass P wave velocity using blasthole drilling information. *Int. J. Min. Reclam. Environ.* **2019**, *33*, 61–74. [[CrossRef](#)]
11. Lakshminarayana, C.R.; Tripathi, A.K.; Pal, S.K. Experimental investigation on potential use of drilling parameters to quantify rock strength. *Int. J. Geo-Eng.* **2021**, *12*, 1–15. [[CrossRef](#)]
12. Alsaihati, A.; Elkhatny, S.; Mahmoud, A.; Abduraheem, A. Use of Machine Learning and Data Analytics to Detect Downhole Abnormalities While Drilling Horizontal Wells, With Real Case Study. *ASME J. Energy Resour. Technol.* **2021**, *143*, 1–15. [[CrossRef](#)]
13. Navarro, J.; Seidl, T.; Hartlieb, P.; Sanchidrián, J.A.; Segarra, P.; Couceiro, P.; Schimek, P.; Godoy, C. Blastability and Ore Grade Assessment from Drill Monitoring for Open Pit Applications. *Rock Mech. Rock Eng.* **2021**, *54*, 3209–3228. [[CrossRef](#)]
14. Liu, H.; Yin, K.K. Analysis and interpretation of monitored rotary blast hole drill data. *Int. J. Min. Reclam. Environ.* **2001**, *15*, 177–203. [[CrossRef](#)]
15. Kosolapov, A.I. Modern Methods and Tools for Determining Drillability and Blastability of Rocks. *IOP Conf. Ser. Earth Environ. Sci.* **2018**, *459*, 022097. [[CrossRef](#)]
16. Kadkhodaie-Ilkhchi, A.; Monteiro, S.T.; Ramos, F.; Hatherly, P. Rock Recognition From MWD Data: A Comparative Study of Boosting, Neural Networks, and Fuzzy Logic. *IEEE Geosci. Remote Sens. Lett.* **2010**, *7*, 680–684. [[CrossRef](#)]
17. Arata, F.; Gangemi, G.; Mele, M.; Tagliamonte, R.L.; Tarchiani, C.; Chinellato, F.; Denichou, J.M.; Maggs, D. High-resolution reservoir mapping: from ultradeep geosteering tools to real-time updating of reservoir models. In Proceedings of the Abu Dhabi International Petroleum Exhibition and Conference, Abu Dhabi, UAE, 7 November 2016; SPE-183133-MS.
18. Wodecki, J.; Góralczyk, M.; Krot, P.; Zietek, B.; Szrek, J.; Worsa-Kozak, M.; Zimroz, R.; Sliwinski, P.; Czajkowski, A. Process Monitoring in Heavy Duty Drilling Rigs—Data Acquisition System and Cycle Identification Algorithms. *Energies* **2020**, *13*, 6748. [[CrossRef](#)]
19. Pastorek, N.; Young, K.; Eustes, A. Downhole Sensors in Drilling Operations. In Proceedings of the 44th Workshop on Geothermal Reservoir Engineering, Stanford, CA, USA, 11–13 February 2019.
20. Pagtalunan, J.; Parmar, K.; Kim, S.; Moon, B.; Park, S.S. Experimental study on repeater-free acoustic telemetry for downhole operations. *J. Petroleum Sci. Eng.* **2021**, *202*, 108551. [[CrossRef](#)]
21. Kianinezhad, R.; Nahid, B.; Betin, F.; Capolino, G.A. Observer-Based Sensorless Field-Oriented control of Induction Machines. In Proceedings of the 2004 IEEE International Symposium on Industrial Electronics, Ajaccio, France, 4–7 May 2004; Volume 2, pp. 1381–1386.
22. Lorenz, R. Future Motor Drive Technology Issues and Their Evolution. In Proceedings of the 12th International Power Electronics and Motion Control Conference, Portoroz, Slovenia, 30 August–1 September 2006; pp. 18–24.
23. Fabri, G.; Olivieri, C.; Tursini, M. Observer-based sensorless control of a five-phase brushless DC motor. In Proceedings of the International Conference on Electrical Machines, Rome, Italy, 6–8 September 2010; pp. 1–6.
24. Observer-Based Motion Control. Available online: <http://www.parkermotion.com/engineeringcorner/doc/ObserverControlArticle.pdf> (accessed on 20 November 2022).
25. Guzinski, J.; Abu-Rub, H.; Diguët, M.; Krzeminski, Z.; Lewicki, A. Speed and Load Torque Observer Application in High-Speed Train Electric Drive. *IEEE Trans. Ind. Electron.* **2010**, *57*, 565–574. [[CrossRef](#)]
26. Mousavi, S.M.; Dashti, G.A. Application of Speed Estimation Techniques for Induction Motor Drives in Electric Traction Industries and vehicles. *Int. J. Automot. Eng.* **2014**, *4*, 857–868.
27. Ramirez, G.; Lorenz, R.D.; Valenzuela, M.A. Observer-based estimation of modulus of elasticity for papermaking process. *IEEE Trans. Ind. Appl.* **2014**, *50*, 1678–1686. [[CrossRef](#)]
28. Tang, L.; He, W.; Zhu, X. The effect of high-frequency torsional impacts on the dynamic response of a drill string in a stick state. *Adv. Mech. Eng.* **2019**, *11*, 1687814019828579. [[CrossRef](#)]
29. Zhang, X.; Luo, Y.; Fan, L.; Peng, J.; Yin, K. Investigation of RC-DTH air hammer performance using CFD approach with dynamic mesh method. *J. Adv. Res.* **2019**, *18*, 127–135. [[CrossRef](#)]
30. Bo, K.; Sun, S.; Hu, Y.; Wang, M. Design Optimization and Performance Analysis of the Pneumatic DTH Hammer with Self-Propelled Round Bit. *Shock Vib.* **2021**, *2021*, 6653390. [[CrossRef](#)]
31. dSPACE-MicroLabBox Product Brochure 2020-01. Available online: <https://www.dspace.com/en/inc/home/products/hw/microlabbox.cfm> (accessed on 20 November 2022).
32. STARTER Commissioning Tool for SINAMICS Converters. Available online: <https://mall.industry.siemens.com/mall/en/ww/catalog/products/10018085> (accessed on 20 November 2022).
33. Bensiali, N.; Etien, E.; Benalia, N. Convergence analysis of back-EMF MRAS observers used in sensorless control of induction motor drives. *Math. Comput. Simul.* **2015**, *115*, 12–23. [[CrossRef](#)]
34. Marwali, M.; Keyhani, A. A Comparative Study of Rotor Flux Based MRAS and Back EMF Based MRAS Speed Estimators for Speed Sensorless Vector Control of Induction Machines. In Proceedings of the Conference Record of the IEEE Industry Applications Conference, New Orleans, LA, USA, 5–9 October 1997; pp. 160–166.

35. 3-Phase AC Induction Motor Vector Control Using DSP56F80x. Available online: <https://www.nxp.com/docs/en/application-note/AN1930.pdf> (accessed on 20 November 2022).
36. Kaltjob, P. *Mechatronic Systems and Process Automation: Model-Driven Approach and Practical Design Guidelines*, 1st ed.; CRC Press: Boca Raton, FL, USA, 2018.
37. *ASTM D7012–14*; Standard Test Method for Compressive Strength and Elastic Moduli of Intact Rock Core Specimens under Varying States of Stress and Temperatures, Annual Book of ASTM Standards. American Society for Testing and Materials: West Conshohocken, PA, USA, 2014.
38. Hoek, E.; Brown, E.T. Practical estimates of rock mass strength. *Int. J. Rock Mech. Min. Sci.* **1997**, *34*, 1165–1186.